Title

Global sphingosine-1-phosphate receptor 2 deficiency attenuates neuroinflammation and ischemic-reperfusion injury after neonatal stroke

Journal

iScience, 26(4)

ISSN

2589-0042

Authors

Fukuzaki, Yumi
Faustino, Joel
Lecuyer, Matthieu
et al.

Publication Date

2023-04-01

DOI

10.1016/j.isci.2023.106340

Peer reviewed

iScience

CellPress
OPEN ACCESS

Article

Global sphingosine-1-phosphate receptor 2 deficiency attenuates neuroinflammation and ischemic-reperfusion injury after neonatal stroke

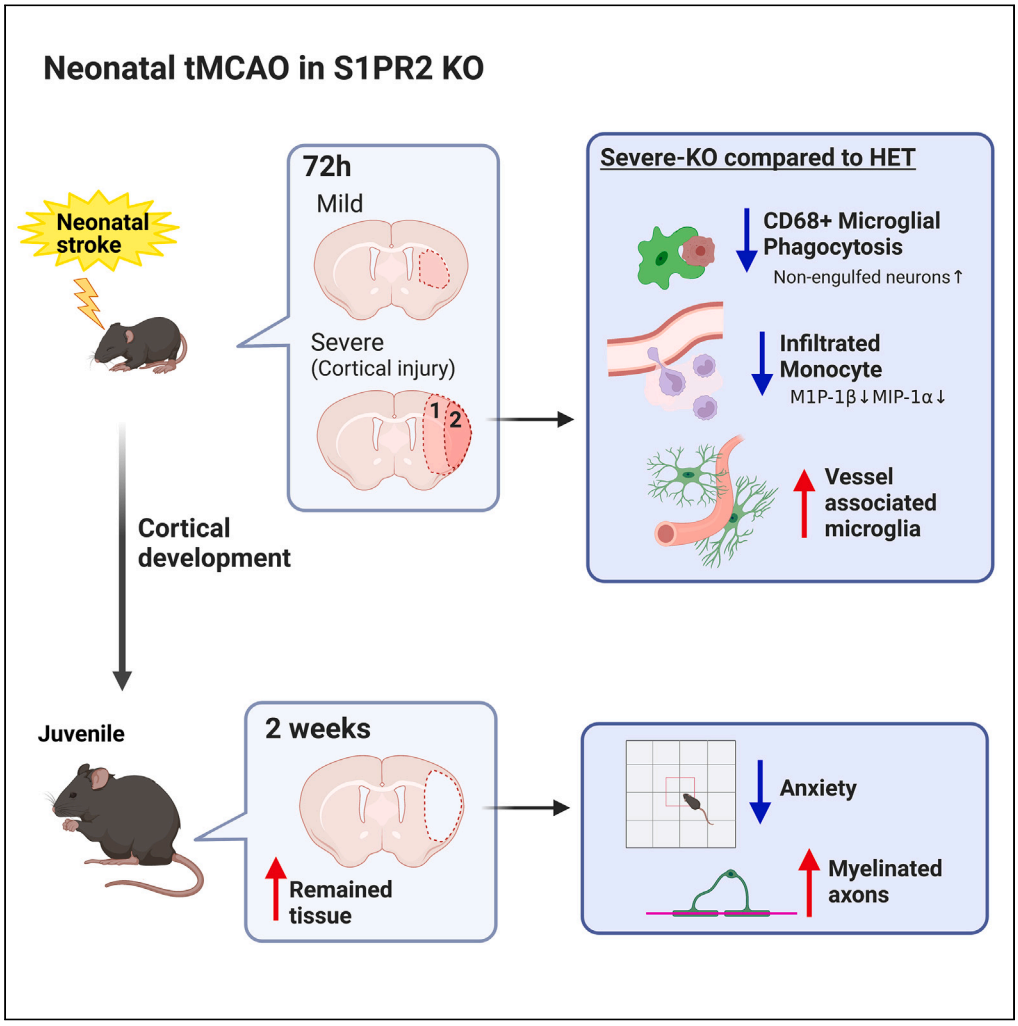

Yumi Fukuzaki, Joel Faustino, Matthieu Lecuyer, Aditya Rayasam, Zinaida S. Vexler

zena.vexler@ucsf.edu

Highlights

Global S1PR2 deletion reduces long-term functional deficits after perinatal stroke

Attenuates acute monocyte infiltration and increases microglia-vessel crosstalk

Reduces anxiety

Enhances brain development in non-affected brain regions

Fukuzaki et al., iScience 26, 106340
April 21, 2023
https://doi.org/10.1016/j.isci.2023.106340

iScience

CellPress
OPEN ACCESS

Article

Global sphingosine-1-phosphate receptor 2 deficiency attenuates neuroinflammation and ischemic-reperfusion injury after neonatal stroke

Yumi Fukuzaki,[1] Joel Faustino,[1] Matthieu Lecuyer,[1] Aditya Rayasam,[1] and Zinaida S. Vexler[1,2,3,*]

SUMMARY

Arterial ischemic stroke is common in neonates—1 per 2,300–5,000 births—and therapeutic targets remain insufficiently defined. Sphingosine-1-phosphate receptor 2 (S1PR2), a major regulator of the CNS and immune systems, is injurious in adult stroke. Here, we assessed whether S1PR2 contributes to stroke induced by 3 h transient middle cerebral artery occlusion (tMCAO) in S1PR2 heterozygous (HET), knockout (KO), and wild type (WT) postnatal day 9 pups. HET and WT of both sexes displayed functional deficits in Open Field test whereas injured KO at 24 h reperfusion performed similarly to naives. S1PR2 deficiency protected neurons, attenuated infiltration of inflammatory monocytes, and altered vessel-microglia interactions without reducing increased cytokine levels in injured regions at 72 h. Pharmacologic inhibition of S1PR2 after tMCAO by JTE-013 attenuated injury 72 h after tMCAO. Importantly, the lack of S1PR2 alleviated anxiety and brain atrophy during chronic injury. Altogether, we identify S1PR2 as a potential new target for mitigating neonatal stroke.

INTRODUCTION

The focus of studies in the adult stroke field has gradually changed from acute neuroprotection to long-term neurorepair.[1,2] Studies of perinatal stroke and hypoxia-ischemia were also predominantly focused on neuronal survival but the mechanisms of neonatal stroke and therapeutic targets continue to be far less known. However, there is now ample evidence that the mechanisms of ischemic injury differ greatly between the immature and adult brain, in part due to the dynamic nature of brain development and associated enhanced brain susceptibility to hypoxia and ischemia-related insults during particular postnatal periods in humans and rodents[3–5] and distinct neuro-immune responses in neonates and adults.[4] In support of brain maturation-dependent differences in focal arterial stroke, we demonstrated that blood-brain barrier (BBB) permeability to several classes of molecules is much lower after acute perinatal stroke than after adult stroke[6] and that receptor-mediated signaling can also differentially contribute to stroke in adult and neonatal mice, as we showed for the scavenger receptor CD36.[7] Modifying a crosstalk between microglia and leukocytes after experimental neonatal arterial ischemic stroke modulates injury.[8–10]

In an adult stroke model, inhibition of an inducible sphingosine-1-phosphate receptor 2 (S1PR2) was demonstrated to be neuroprotective,[11] in part by modifying the microglia-leucocyte axis. Expression of S1PR1 and S1PR2 in microglial cells is high[12] and S1PR1-5 regulates the function of the peripheral immune system and cerebral vessels,[13,14] making it plausible that protection may occur via modification of the microglia-leucocytes axis.

Knowing that the contribution of individual receptors to stroke severity can differ between neonates and adults, in this study, we examined the role of S1PR2 in sub-acute and chronic injury after a transient middle cerebral artery occlusion (tMCAO) in neonatal S1PR2 heterozygote (HET) mice and mice with global S1PR2 knockout (KO), focusing on functional and histological outcomes and on several features of inflammation,[4] including inflammation as manifested by cytokine accumulation, activation of microglia, the main immune cell type in the brain, and on phenotypes of peripheral myeloid cells. Leukocytes can mediate injury upon their recruitment to the post-ischemic region and without infiltrating into the brain, by releasing cytokines while loosely attached to endothelial cells during acute reperfusion after tMCAO or via blood-CSF barrier.[9] Using both the genetic approach (KO) and pharmacological approach- by administration of an S1PR2

[1]Department of Neurology, University California San Francisco, Weill Institute for Neurosciences, San Francisco, CA 94158-0663, USA

[2]Senior author

[3]Lead contact

*Correspondence: zena.vexler@ucsf.edu

https://doi.org/10.1016/j.isci.2023.106340

inhibitor JTE-013 beginning at reperfusion- we demonstrate reduced infiltration of inflammatory monocytes and improved functional outcome during sub-chronic injury phase as well as improvement in functional outcome, reduced tissue loss, and improved postnatal cortical development in the contralateral hemisphere 2 weeks after neonatal tMCAO.

RESULTS

Global S1PR2 knockout attenuates functional deficits after sub-chronic tMCAO in neonatal mice

We previously showed that transient 3 h MCAO in neonatal mice leads to consistent substantial injury that includes both the cortex and the caudate,[7,8] region- exclusively supplied by the MCA. Here we asked if lack of S1PR2 affects the severity of injury. Volumes of contralateral and ipsilateral hemispheres were similar in WT, HET, and KO pups 72 h after tMCAO (Figures 1A and 1B). Injury volumes were consistent in WT and HET groups (Figure 1C). In contrast, two patterns of injury were apparent in the KO group (Figure 1C), a severe injury that included both the cortex and the caudate was observed in 7/12 pups, whereas milder injury limited to the caudate was observed in 5/12 pups (Figure 1C). In both subgroups, injury volume was similar in male and female pups (Figure 1C′).

Next, we investigated if lack of S1PR2 affects functional deficits 24 h after reperfusion. Representative trajectories in Open Field test are shown in Figure 1D, left. Total traveling distance was similar in naive WT, HET, and KO (Figure 1D, right). Compared to naive HET, total travel distance was significantly reduced in HET pups subjected to tMCAO. Based on the presence of two injury patterns in KO (Figure 1C), we examined total distance traveled separately in both subgroups, focusing on severely injured KO. Total distance traveled by KO with severe injury remained at levels observed in naive KO (Figure 1D) and was significantly longer than by injured HET. Total distance by KO with mild injury was similar to that in both naive and severely injured KO (Figure 1D′). No sex differences were apparent (Figure 1D″).

Considering significantly different locomotion yet similar injury volumes in HET and severely injured KO mice, we further characterized injury by examining the extent of cleaved caspase3 (Cl.casp3)-dependent and calpain-dependent fragmentation of the α-spectrin chain (Figures 1E–1H). Consistent with previous reports in WT pups,[15–17] tMCAO triggered both casp3-dependent (Figure 1G) and calpain-dependent (Figure 1H) α-spectrin fragmentation but both types of spectrin degradation were significantly lower in KO than in HET mice (Figures 1G and 1H), indicating attenuation of both casp3-dependent and independent neuronal injury in ischemic-reperfused regions. Knowing that S1PR1 can counteract the effects of S1PR2 after stroke,[11] we examined S1PR1 expression in the same pups. tMCAO led to marked similar downregulation of S1PR1 in injured regions regardless of whether S1PR2 was present (Figure 1I).

Pharmacological inhibition of S1PR2 protects the neonatal brain from sub-chronic injury after tMCAO

We then examined the effects of pharmacological inhibition of S1PR2 in WT pups administered S1PR2 antagonist JTE-013 daily beginning 1 h after reperfusion. Compared to vehicle-treated pups, 72 h after tMCAO injury volume was significantly decreased in pups treated with each of two doses tested, 2.5 μg/g and 5 μg/g (Figures 2A and 2B). Given a similar magnitude of injury attenuation by both JTE-013 doses, we limited further testing to a lower dose. Casp3-dependent fragmentation of the α-spectrin chain was significantly increased in injured regions of vehicle-treated but not in injured regions of JTE-013 treated pups (Figures 2C and 2D). Calpain-cleaved fragmentation was induced by tMCAO but was similar in JTE-013- and vehicle-treated groups (Figure 2E). Therefore, each approach, global S1PR2 deletion or pharmacological inhibition of S1PR2 after tMCAO, attenuated spectrin degradation and thus, injury, during the sub-chronic injury phase.

Lack of S1PR2 preserves neurons in injured region

Knowing that diminished removal of dying neurons in neonatal ischemic-reperfused brain exacerbates injury and can lead to a secondary inflammatory response,[7] we examined the effects of S1PR2 deletion on the number of $NeuN^+$ neurons and neuronal phagocytosis by $CD68^+$ microglia/macrophages in four field-of-view(s) (FOV)s, including regions not directly supplied by the MCA (FOV 1), perifocal region (FOV 2), and in two FOVs within the ischemic core (Figure 3A), closer to formed astrocytic glial scar (FOV 3) and farther from glial scar (FOV 4) in severely injured mice (Figures 3A–3C), or in same morphologic

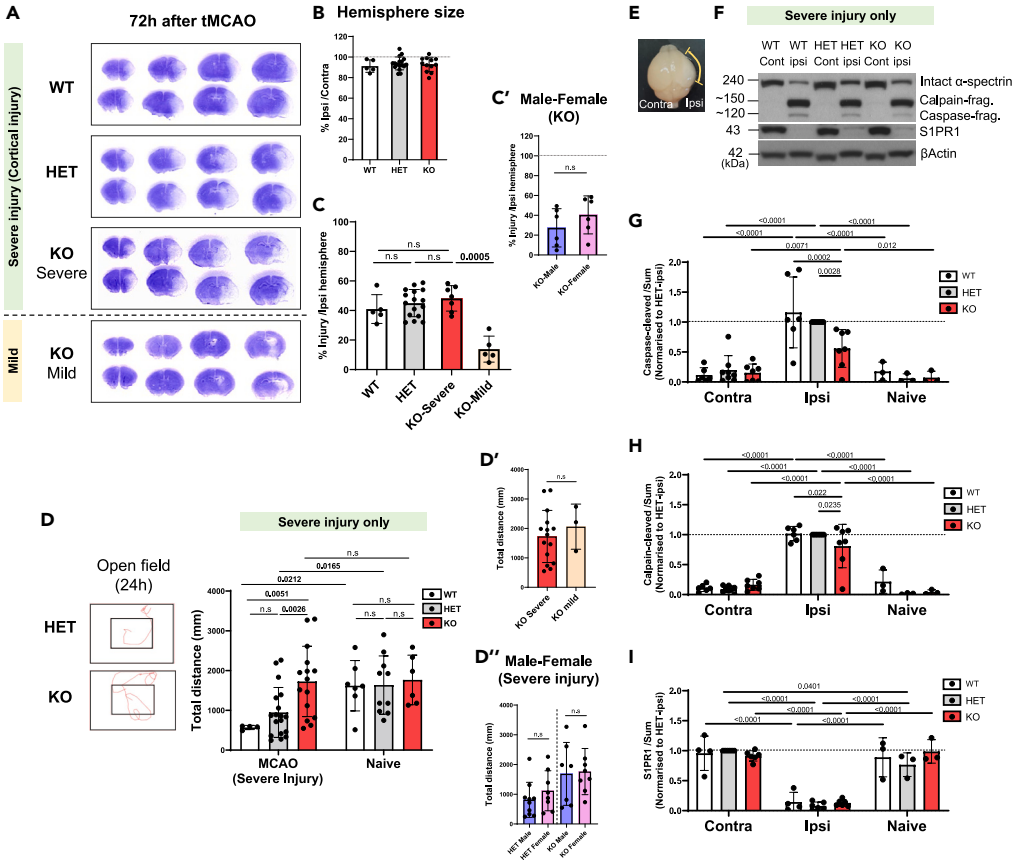

Figure 1. Global S1PR2 KO deletion attenuates functional deficits 72 h after tMCAO in neonatal mice

(A–C) (A) Representative images of Nissl-stained coronal brain sections 72 h after tMCAO in WT, HET, and KO. Discolored area depicts area with massive neuronal death. For KO group, images of both severely injured brain that involve- both the cortex and the caudate (image second from the bottom) and more mildly injured brain, with injury limited to the caudate ipsilateral to tMCAO (bottom image). (B) Quantification of hemispheric size (shown as percent of volume of ipsilateral hemisphere relative to volume of contralateral hemisphere). (C) Quantification of injury volume (shown as percent of injury volume per volume of ipsilateral hemisphere). The groups were separated based on the injury extent and pattern, severe (cortical injury) and mild (non-cortical injury) in KO. Insert C′ demonstrates similar injury volume in severely injured KO males and females (M/F).

(D) Examples of trajectories of total locomotion distance in the Open Field test 24 h after tMCAO (left) and quantification of total distance over 3 min in naive pups and pups subjected to tMCAO (right). Note that shown are data for pups designated for both histological outcomes (Figures 1A–1C) and for biochemical outcomes (Figures 1E–1H). D′ total distance in severe- and mild-injury in KO. D″ demonstrates that there are no sex differences in the Open Field test between severely injured KO and HET.

(E–I) Whole brain showing severe injury (yellow arrow) (E). Representative images of Western blot in lysates from injured and contralateral regions. (F). Quantification of caspase-dependent fragmentation of alfa-spectrin chain. (G). calpain-dependent fragmentation of alfa-spectrin chain. (H). S1PR1 expression in WT, HET, and KO. (I). Data shown as mean ± SD. Each dot in B–D and G–I represents data from an individual mouse. Two-way ANOVA followed by two-stage step-up method of Benjamini, Krieger, and Yekutieli was used to compare multiple groups with independent variables (D, G–I), one-way ANOVA followed by Brown-Forsythe and Welch ANOVA was used for B–C, and *t*-test (parametric) or Mann Whitney test (nonparametric) were used to compared two groups (C′, D′, D″). Statistical values are indicated on individual panels.

regions of KO with mild injury and matching contralateral regions. Massive neuronal death was apparent in both FOV 3 and FOV 4 of HET and in severely injured KO (Figures 3B and 3C). Compared to the density of $NeuN^+$ cells in injured regions of HET mice, the density of $NeuN^+$ cells was significantly higher in the entire KO cohort (Figure 3D) and in pups with severe injury (Figure 3D′), while the numbers of $Cl.casp3^+$ cells (Figures 3E and 3E′) and $CD68^+$ cells (Figures 3F and 3F′) were similar in HET and KO. There were no sex differences in $NeuN^+$, $CD68^+$, or $Cl.casp3^+$ cells in severely injured KO compared to HET (see

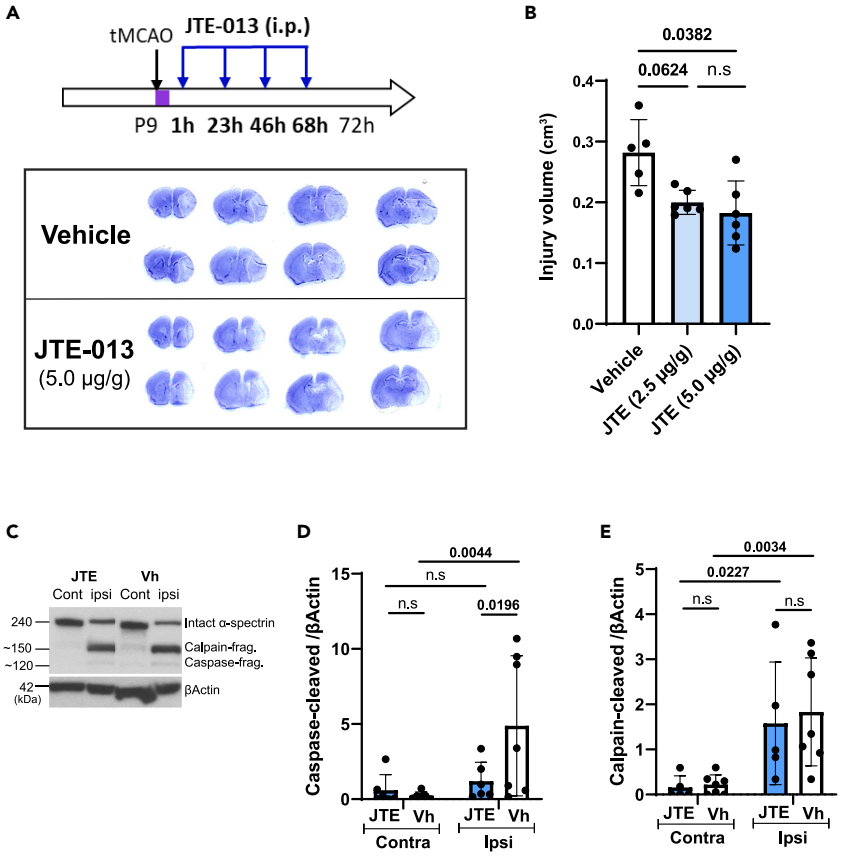

Figure 2. Effect of S1PR2 inhibition on injury 72 h after reperfusion

(A and B) Experimental protocol of tMCAO and intra-peritoneal administration of vehicle/JTE-013 (A) and injury size in Nissl-stained brains (B).

(C–E) Representative image of a Western blot (C) and quantification of cleavage of α-chain spectrin by caspase-3 (120 kDa band, D) and by calpain (150 kDa band, E). Data shown as mean ± SD. Each dot represents data from an individual mouse. Two-way ANOVA was used to compare multiple groups with independent variables followed by two-stage step-up method of Benjamini, Krieger, and Yekutieli (D–E), and one-way ANOVA followed by Brown-Forsythe and Welch ANOVA tests was performed in B. Statistical values are indicated on individual panels.

Supplemental Figures S1A–S1C). The number of engulfed neurons by CD68$^+$ cells was similar in HET and KO regardless of injury (Figures 3G and 3G′), whereas the number of non-engulfed neurons was significantly higher in the entire KO cohort (Figure 3H) and in severely injured KO (Figure 3H′). KO pups that did not have injury in the cortex (i.e., mild injury) showed no sign of microglial morphological transformation. Neuronal density was much higher in those pups than severely injured KO pups or HET pups (see Supplemental Figures S1D–S1E).

Further characterization of the effects of S1PR2 deficiency on injury by evaluation of reactive astrocytosis showed similar volumes of GFAP$^+$ coverage (Figure 3J) in both groups. Although vessel coverage was similar in HET and KO mice in contralateral and ipsilateral regions adjacent to injury (Figures 3K–3L), the density of vessel-associated microglia/macrophages was significantly higher in KO than in HET pups (Figures 3K and 3M). Cumulatively, these data suggest that global S1PR2 deficit protects neurons in the ischemic core and increases microglia/macrophage–vascular associations adjacent to the injury.

tMCAO triggers accumulation of chemokines in injured regions of S1PR2 HET and S1PR2 KO neonates

tMCAO significantly increased levels of several chemokines (Figure 4A) and cytokines (Figure 4B) in HET and KO in injured regions compared to respective levels in matching contralateral hemispheres. In

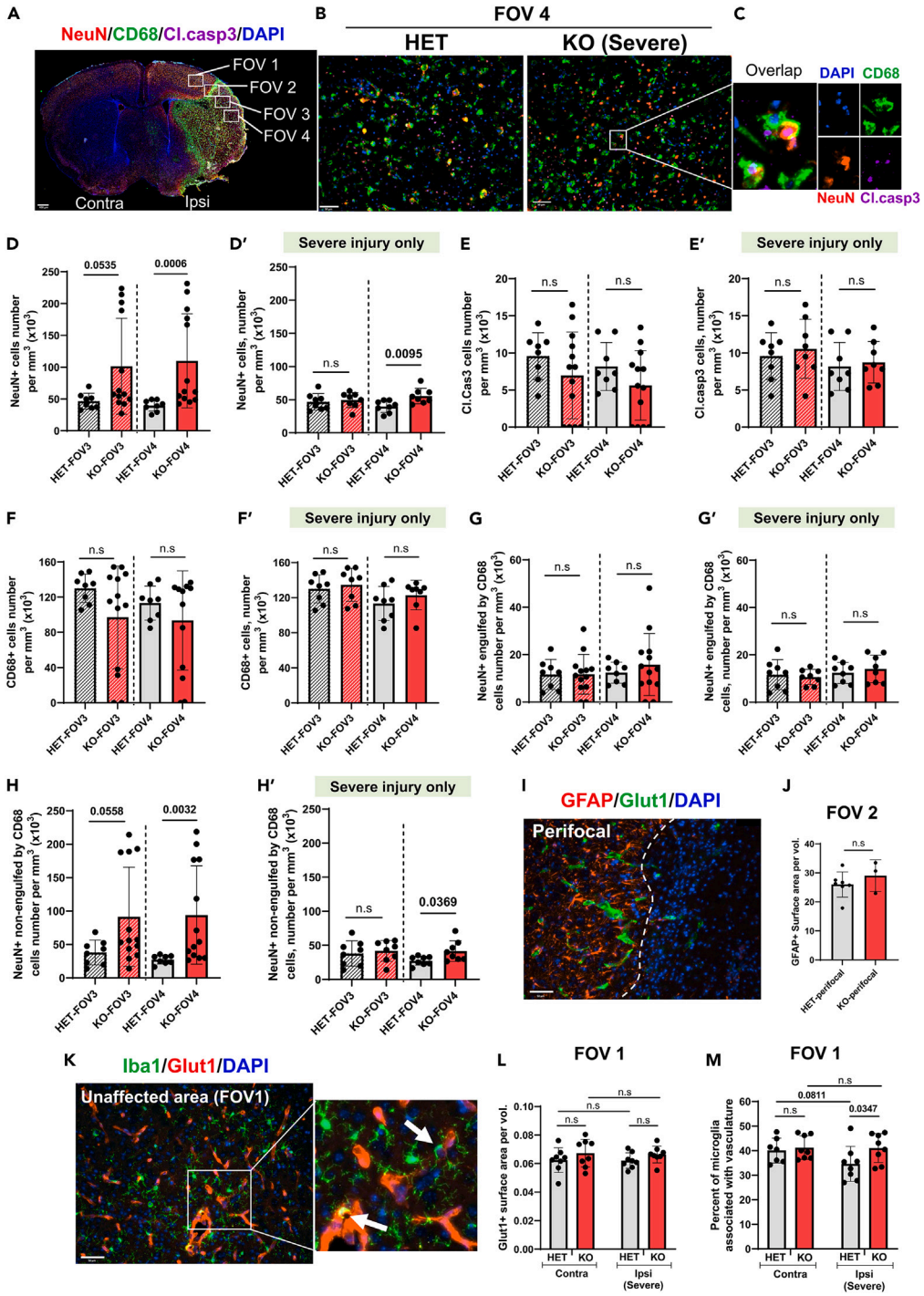

Figure 3. Lack of S1PR2 enhances neuronal survival in the ischemic core and affects microglia-vascular associations in perifocal region 72 h after tMCAO

(A) A diagram that demonstrates areas for image acquisition in B–C, I and K. Note that FOV 1 outlines region outside of the vascular territory supplied by the MCAO, FOV 2 outlines typical penumbral region and FOV 3/4 corresponds to the ischemic core in severely injured pups. Scale bar, 400 μm.

(B–H) (B). Immunofluorescence image of NeuN+ (red), $CD68^+$ (green) cells and cells with cleaved caspase 3 (Cl.casp3; purple) in the ischemic core (FOV 3 and 4; identified by DAPI appearance). Scale bar, 50 μm. (C). Magnified image from B. Density of NeuN+ neurons (D), Cl.casp3+ neurons (E), $CD68^+$ cells (F), NeuN+ neurons engulfed by $CD68^+$ cells (G), and

Figure 3. *Continued*

non-engulfed neurons (H) in FOV 3 and FOV 4 of the entire cohorts of pups that underwent tMCAO. Plots 3D′, 3E′, 3F′, 3G′ and 3H′ show respective densities in severely injured KO only (see Figure 1C′) and in all injured HET (see Figure 1C′).

(I and J) (I). Representative image of GFAP+ reactive astrocytes and GLUT1+ vessels. Scale bar, 50 μm. (J). Quantification of surface area coverage by GFAP+ cells.

(K–M) (K). Representative image of microglia associated with GLUT1+ vessels (white arrow) adjacent to injury. Scale bar, 50 μm. (L). Quantification of Glut1+ surface area. (M). Percent of microglia associated with the vasculature. Data shown as mean ± SD. Each dot represents data from an individual mouse. Two groups were compared by *t*-test or Mann Whitney test in D–J and two-way ANOVA was used to compare multiple groups with independent variables followed by two-stage step-up method of Benjamini, Krieger, and Yekutieli (L, M). Statistical values are indicated on individual panels.

particular, levels of interleukins IL-1α, IL-6, IL-12 (p40), and G-CSF and chemokines MIP-1β and MIP-1α were significantly higher in injured regions of HET and KO pups compared to respective contralateral regions, but the magnitude of increase was similar in two groups. The levels of GM-CSF and TNFα were not significantly affected by injury, consistent with our previous observations in WT mice.[7,16] Lack of S1PR2 reduced only the level of MIP-1β and MIP-1α (Figure 4A). Considering that MIP-1β and MIP-1α may contribute to leukocyte recruitment into inflammatory sites, we next investigated infiltration of leukocytes into injured regions.

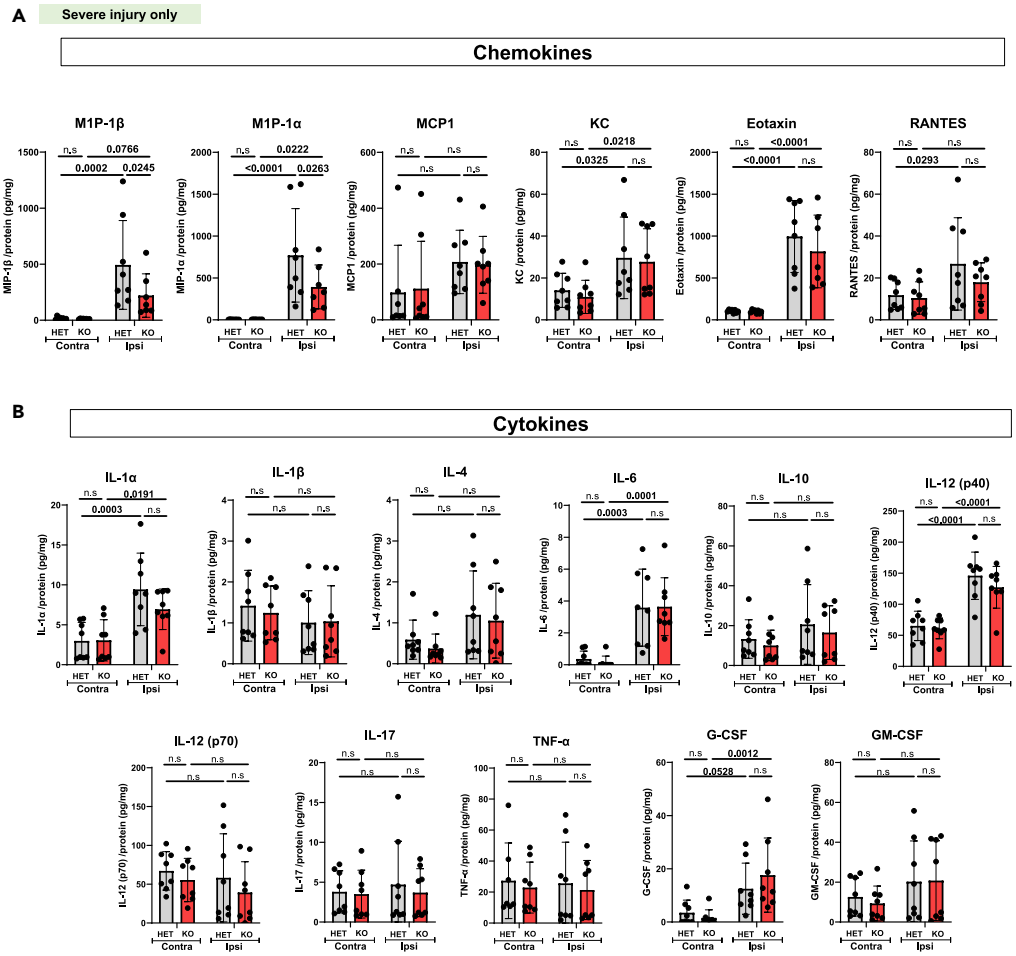

Figure 4. Effects of tMCAO on cytokine and chemokine accumulation in injured HET and KO pups

(A–E) Chemokine/cytokine levels 72 h after tMCAO. The levels of individual chemokines (A) and cytokines (B) in contralateral and injured cortex in HET and KO. Data shown as mean ± SD. Each dot represents data from an individual mouse. Two-way ANOVA was used to compare multiple groups with independent variables followed by two-stage step-up method of Benjamini, Krieger, and Yekutieli. (A–B). Statistical values are indicated on individual panels.

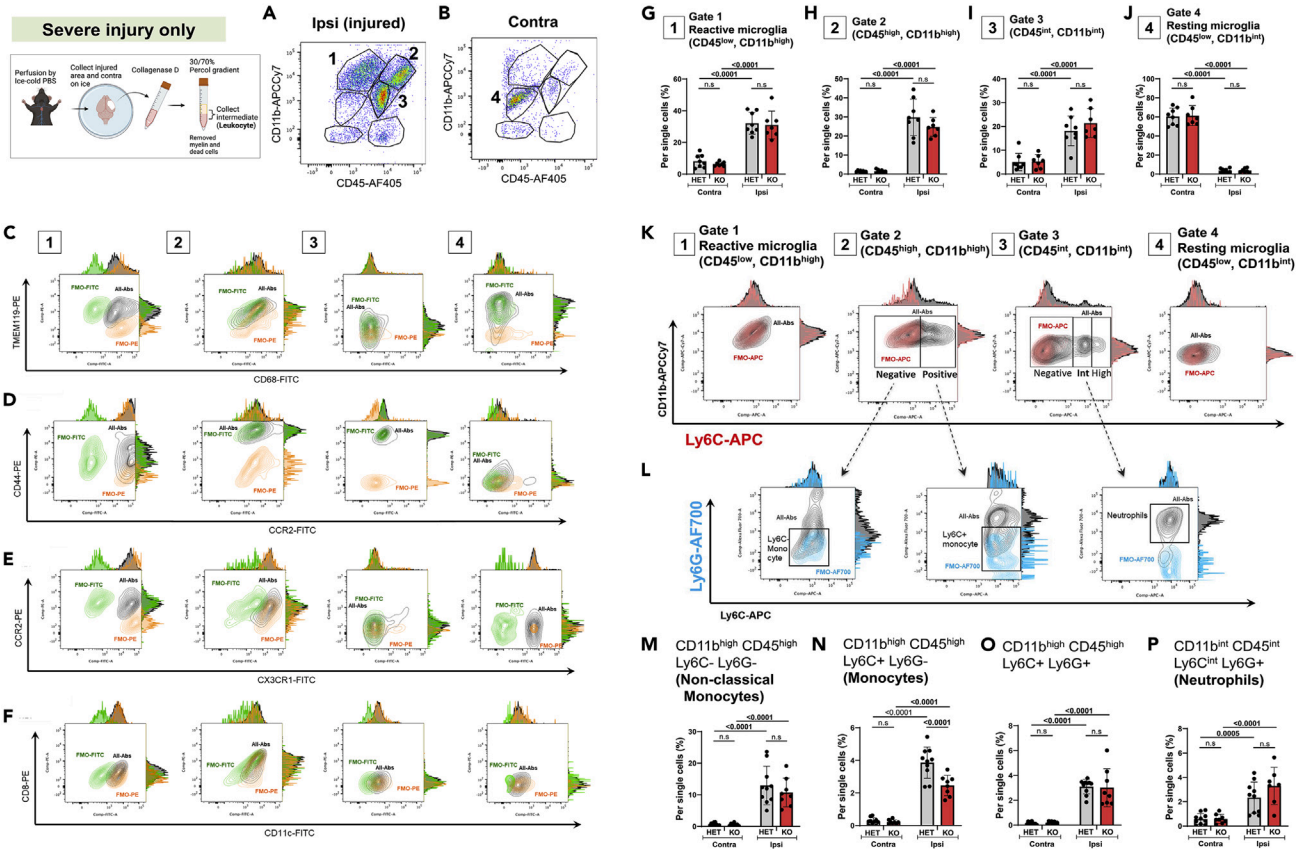

Figure 5. Effects of S1PR2 deletion on microglial phenotypes and patterns of infiltrated peripheral leukocytes72 h after tMCAO. Top left: A diagram demonstrates isolation of cells

(A and B) Flow cytometry gating strategy to identify individual subpopulations of leukocytes and microglia in injured (A) and matching contralateral regions (B). Gates 1–4 were selected based on the patterns of CD11b-APCCy7 and CD45-AF405 staining.

(C–F) Representative plots of cell populations in Gates 1–4 based on the following combinations of specific markers: TMEM119-PE/CD68-FITC (C), CD44-PE/CCR2-FITC (D), CCR2-PE/CX3CR1-FITC (E), and CD8-PE/CD11c-FITC (F). Gates 1–4 are shown as numbers 1–4 in boxes above plots. Color code to individual FMOs: PE (orange), FITC (green), and all-antibodies (Abs; black). Adjustment histogram is shown in each X-Y axis.

(G–J) Quantification of cell number per single cell population in Gates 1–4. $CD45^{low}$, $CD11b^{high}$ (G, Gate 1), $CD45^{high}$, $CD11b^{high}$ (H, Gate 2), $CD45^{int}$, $CD11b^{int}$ (I, Gate 3), and $CD45^{low}$, $CD11b^{int}$ (J, Gate 4).

(K–L) Representative plots for Ly6C-APC (K) from Gates 1–4 and further gating on Ly6G-AF700 (L) to discriminate monocytes and neutrophils. FMOs: Ly6C-APC (red) and Ly6G-AF700 (blue), and all-Abs (black). Gate 2 ($CD45^{high}$, $CD11b^{high}$) separated into negative/positive by Ly6C-APC (K, Left). Gate 3 ($CD45^{int}$, $CD11b^{int}$) separated into three populations (negative, intermediate, and high) in Ly6C-APC(K, second from left). Further, these are gated by Ly6G-AF700 (L). Adjustment histogram is shown on each plot.

(M–O) Analysis of cell populations. $CD11b^{high}CD45^{high}$ $Ly6C^{-}Ly6G^{-}$ non-classical monocytes (M), $CD11b^{high}CD45^{high}$ $Ly6C^{+}Ly6G^{-}$ monocytes (N), $CD11b^{high}CD45^{high}$ $Ly6C^{+}Ly6G^{+}$(O).

(P) Analysis of cell populations $CD11b^{int}CD45^{int}Ly6C^{+}Ly6G^{+}$ neutrophils. Data shown as mean ± SD. Each dot represents data from an individual mouse. Two-way ANOVA was used to compare multiple groups with independent variables followed by two-stage step-up method of Benjamini, Krieger, and Yekutieli (G–J, M–P). Statistical values are indicated on individual panels.

The number of infiltrated monocytes is decreased in S1PR2 KO neonates 72 h after tMCAO

To further examine the effects of S1PR2 deletion on neuroinflammation after neonatal stroke, we characterized microglial activation and leukocyte infiltration by flow cytometry 72 h after tMCAO in HET and KO pups with severe injury, gating on $CD11b^{+}/CD45^{+}$ cells (Figures 5A and 5B). There were three $CD11b^{int\text{-}high}$ cell populations in the injured cortex (Gates 1–3, Figure 5A) and one $CD11b^{int}$ population in the contralateral cortex (Gate 4, Figure 5B). To identify cell types in these populations, cells were stained with several cell surface markers and the FMO approach was used to define the cutoff in each channel.[18] Table 1 summarizes individual cell populations. Cells in Gate 1 and Gate 4 were positive for specific microglial marker TMEM119, whereas only cells in Gate 1 were positive for a lysosomal marker CD68, suggesting that cells in Gate 1 were activated microglia/macrophages, whereas cells in Gate 4 were resting microglia

Table 1. Summarized individual cell populations in flow cytometry gates 1-4

Cell surface marker	Gate 1	Gate 2	Gate 3	Gate 4
CD45	Low	High	Int	Low
CD11b	High	Int	High	Int
CD68	+	–/+	–	–
TMEM119	+	–	–	+
CD44	Low	High	High	–
CX3CR1	+	+	–	+
CCR2	+	–/+	–/+	–
CD11c	Low	–	–/+	Low
CD8	–	–	–	–
Ly6C	–	–/+	-/Int/High	–
Ly6G		–/+	–/+	

(Figure 5C). Cells in Gate 2 and Gate 3 were negative for TMEM119 (Figure 5C) but had high CD44 expression (CD44^{high}, Figure 5D), suggesting infiltrated leukocytes as origin. Cells in Gate 2 were CX3CR1^{+}, suggesting monocyte lineage as origin (Figure 5E). In the contralateral cortex, cells were CD45^{low}/CD11b^{int}/TMEM119^{+}/CD68^{-}, consistent with the appearance of resting microglia (Figures 5B and 5J). In the injured cortex, the number of activated microglia/macrophages defined as CD45^{low}/CD11b^{high}/TMEM119^{+}/CD68^{+} cells (Gate 1, Figures 5A and 5G), was significantly higher in HET and KO. The number of CD45^{high}/CD11b^{int}/TMEM119^{-}/CD68^{-}/CD44^{high}/CX3CR1^{+} cells (Gate 2, Figures 5A and 5H) and CD45^{int}/CD11b^{high}/TMEM119^{-}/CD68^{-}/CD44^{high}/CX3CR1^{-} (Gate 3, Figures 5A and 5I) was also significantly higher in injured regions of both HET and KO mice.

Subdivision of CD45^{+}/CD11b^{+} cells based on the expression of Ly6C (Figure 5K) and Ly6G (Figure 5L) showed a significantly lower number of Ly6C^{+}/Ly6G^{-} inflammatory monocytes in the injured region of KO compared to HET mice (Figure 5N), whereas the number of non-classical Ly6G^{-}Ly6C^{-} monocytes (Figure 5M), Ly6G^{+}Ly6C^{+} neutrophils (Figure 5O) and Ly6G^{+}Ly6C^{-} cells (Figure 5P) was unaffected. These data suggest that multiple subtypes of peripheral leukocytes are recruited to injured regions of HET and KO mice, while recruitment of only inflammatory monocytes is reduced in injured KO mice.

Lack of S1PR2 attenuates anxiety and tissue loss 2 weeks after tMCAO

Given the beneficial effects of S1PR2 deletion on functional outcomes and changes in immune signaling early after tMCAO, we then investigated effects on longer-term behavioral outcomes. Open Field test performed 2 weeks after tMCAO showed long-lasting behavioral deficits in injured HET mice, as manifested by significantly reduced relative time spent within center quadrants compared to that in naive HET mice and KO after tMCAO (Figure 6B). Total distance traveled by injured HET remained unchanged compared to naive HET (Figure 6C). In contrast, percent distance in the center and total distance travelled remained unchanged in injured KO mice compared to naive KO (Figures 6B and 6C). The grooming and rearing behavior remained unchanged in both HET and KO groups (Figures 6D and 6E). Based on the shorter distance traveled in the center, anxiety was increased in injured HET but not KO.

Tissue loss was apparent in both groups (Figure 6F) but volume of remaining tissue was significantly larger in injured KO than in HET (Figure 6G). The size of the contralateral hemisphere was also significantly larger in KO pups (Figure 6G). Cortical thickness in secondary motor cortex (MOs) was also larger in contralateral KO compared to HET (Figure 6H). Based on morphological evaluation, Iba1^{+} cells were resting microglial cells in peri-infarct area (Figures 7B and 7C). Density of Iba1^{+} cells was higher in injured KO than in injured HET mice (Figure 7D), but proliferation of microglia (BrdU^{+}/Iba1^{+} cells) was similar (Figure 7E). Density of microglia associated with vessels was significantly higher in injured KO than in injured HET mice (Figure 7F). Vessel volume and endothelial proliferation were unaffected by lack of S1PR2 (Figures 7G and 7H), and no signs of direct effects on neurogenesis were apparent based on density of DCX^{+}/BrdU^{+} cells (Figure 7J and 7K) in the ipsilateral SVZ. These data suggest that S1PR2 deficiency affects microglia-vessel crosstalk in injured pups but does not have direct effects on neurogenesis.

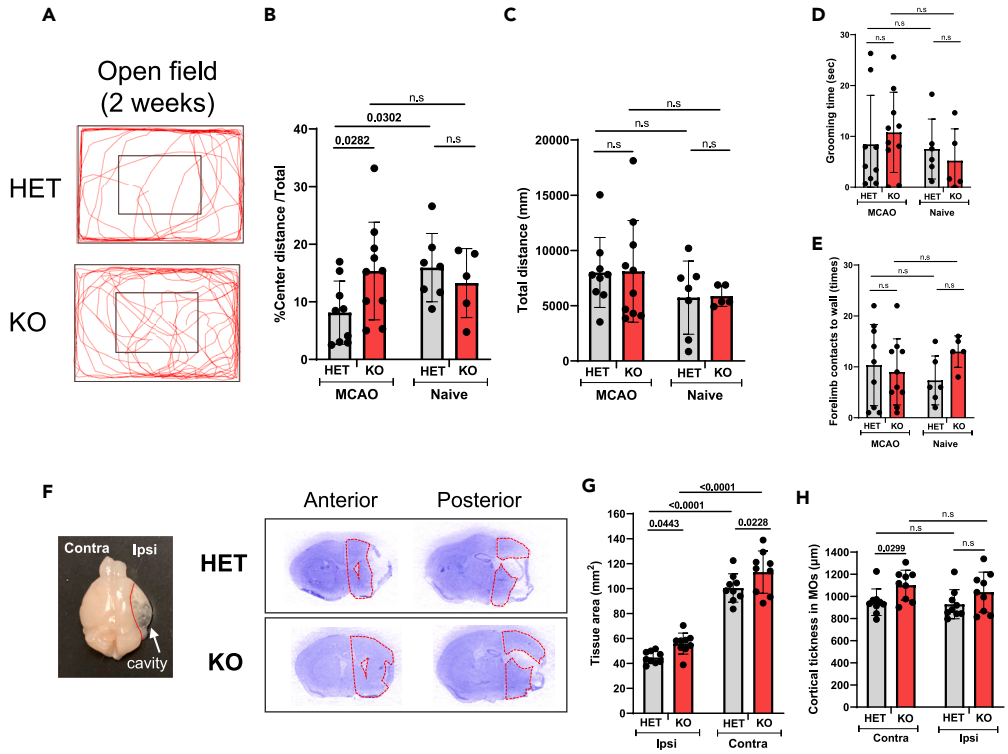

Figure 6. Global S1PR2 deletion contributes to long-term recovery after tMCAO in neonatal mice

(A–E) Effects of S1PR2 deletion on behavior in Open Field test in P21 HET and KO. (A) Examples of traveling trajectory and distance 2 weeks after tMCAO by HET and KO (red line). (B) Total distance, (C) percent of traveling distance in the center per total distance, (D) self-grooming time, and I total time for forelimb contact to the wall over first 2–3 min.

(F–I) (F) Representative images of Nissl-stained coronal sections 2 weeks after tMCAO. Red dash lines outline remaining tissue in hemisphere ipsilateral to the occlusion. (G) Quantification of cortical thickness in MOs (H). Data shown as mean ± SD. Each dot represents data from an individual mouse. Two-way ANOVA was used to compare multiple groups with independent variables followed by two-stage step-up method of Benjamini, Krieger, and Yekutieli (B-E, G-H).

Finally, we examined whether S1PR2 deletion affects myelination of neurofilaments and cortico-cortical projection neurons in proximity to perifocal region and the matching contralateral regions. Neurofilament enwrapment by myelin (area of co-localized MBP^+/NF^+) was smaller in contralateral regions of HET than in contralateral regions of KO (Figure 7M) or naive HET pups (Figure 7M), also coverage of pan-NF (Figure 7N) and MBP^+ (Figure 7O) was smaller in contralateral region of HET and KO pups. Callosal projection neurons were shown to extend axons bilaterally in the motor cortex (MO) throughout development, with dual projections occurring at P8 and refining until around P21 in mice.[19,20] At 2 weeks after tMCAO, FOXP2/NeuN immunolabeling showed a trend in higher percentage of $FoxP2^+$ projection neurons per $NeuN^+$ population in secondary motor cortex between genotypes ($p = 0.1$; FOV1, MOs), whereas no difference was observed in the primary motor cortex (FOV2, MOp) in the ipsilateral cortex. These data suggest that neonatal stroke affects cortical development in the region not directly affected by the tMCAO (Figure 7Q). Taken together, S1PR2 deficiency attenuated anxiety and tissue loss as well as improved postnatal cortical development in the remaining tissue at 2 weeks after neonatal tMCAO.

DISCUSSION

We show that S1PR2, a receptor that plays a key role in mediating vascular inflammation, contributes to injury after neonatal stroke, as both global deletion of S1PR2 and its pharmacologic inhibition improve functional outcomes during sub-chronic and chronic injury phases. Protection occurs in part by attenuating infiltration of inflammatory monocytes into ischemic-reperfused region and altered vessel-microglia interactions in the injured cortex, but, interestingly, without major attenuation of cytokine and chemokine accumulation in injured regions. We also demonstrate that pharmacologic inhibition of S1PR2 after tMCAO attenuates sub-chronic injury.

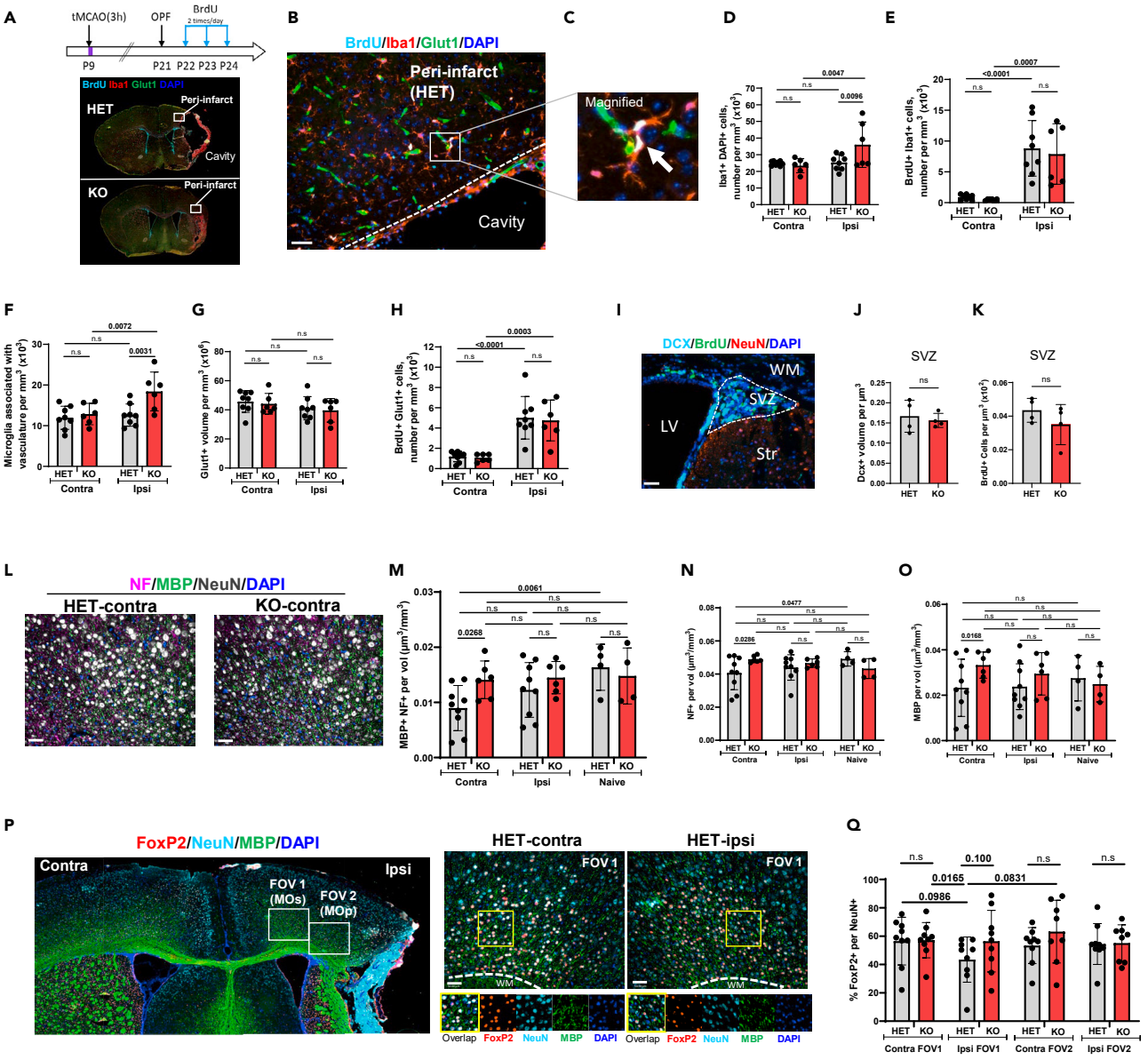

Figure 7. Effects of S1PR2 deficiency on microglial-vascular associations and axonal myelination 2 weeks after tMCAO

(A–H) Microglial and endothelial proliferation 2 weeks following tMCAO. (A) BrdU administration protocol (top) and low magnification images outlining FOV for image acquisition. Scale bar, 800 µm. (B–C) Immunofluorescence images in peri-infarct region (B) and magnified image of microglia associated with vasculature (C, white arrow). Scale bar, 50 µm. Quantification of (D) density of BrdU+/Iba1+ cells, (E) Iba1+/DAPI+ cells, (F) density of microglia associated with the vasculature, (G) volume of the vasculature and (H) BrdU+/Glut1+ cells.

(I–K) Accumulation of DCX+ cells in the SVZ. (I) Image and (J) volume occupied by DCX+ cells and (K) density of BrdU+ in SVZ.

(L–O) (L) Representative images of NF+, MBP+, NeuN+ cells. Quantification of volume of (M) MBP+/NF+, (N) NF + cells and (O) MBP+ per FOV.

(P–Q) (P) Representative low magnification image of areas for FoxP2+, MBP+ NeuN+, DAPI+ image acquisition (left, Scale bar, 300 µm) and higher magnification images (right, Scale bar, 50 µm). (Q) Quantification of FoxP2+/NeuN+ cells. Data shown as mean ± SD. Each dot represents data from an individual mouse. Two-way ANOVA was used to compare multiple groups with independent variables followed by two-stage step-up method of Benjamini, Krieger, and Yekutieli (D-H, M-O, Q). Mann Whitney test was performed to compare two groups (J-K).

Bioactive sphingolipids and their synthetizing/metabolizing enzymes mediate many physiological processes. An imbalance within sphingolipid "rheostat" serves as a prerequisite to developing pathological states,[14] including stroke.[21] S1P regulates intracellular metabolism and neurovascular and immune systems by acting via its G-protein coupled receptors S1PR1-5.[14,22] S1PR1 and S1PR3 act as major regulators of

T cell and B cell trafficking, whereas S1PR2 plays a key role in mediating vascular inflammation,[22] disrupting cerebrovascular integrity and limiting angiogenesis in stroke.[11]

Our data demonstrate severe consistent histological outcome 72 h after tMCAO in HET and WT pups in this study, consistent with our previous findings in WT pups on the same genetic background.[7,8,16] In contrast, histological analysis revealed two subgroups within the KO group, one subgroup with severe injury and associated marked microglia activation (58% KO) and another with injury limited to the caudate and lack/minor signs of microglial activation (42% KO). We did not lump the two KO subgroups together and focused only on severely injured KO subgroup as a translationally relevant approach, as studies in human neonates with hypoxic-ischemic encephalopathy (HIE) and arterial stroke demonstrate that the severity of initial injury critically affects responsiveness to therapeutic approaches,[23] justifying the need to study infants with severe and moderate injury separately. We demonstrate long-lasting improved functional outcome in KO pups with severe injury. Although stroke is more common in male than in female neonates,[24,25] mechanisms of neuronal death are sex-dependent in (hypoxia-ischemia) H-I[26,27] and responses to anti-inflammatory therapies after perinatal brain injury can be sex-dependent,[28,29] we did not observe sex differences in behavior outcome or injury volume. There were also no sex differences in the number of surviving neurons or density of $CD68^{+}$ microglia/macrophages following sub-acute injury.

Studies in adult stroke[11] and germinal matrix in premature infants[30] reported injurious effects of S1PR2 to occur via inducing vascular inflammation without affecting immune cell trafficking,[22] but the role of microglial/macrophage interactions has been largely overlooked. Yet, such interactions may offer new perspectives for treatment of neurodegenerative diseases.[31] Our previous study revealed that the presence of microglial cells prevents hemorrhagic transformation and BBB leakage after tMCAO in neonates,[8] suggesting the critical role of microglia in supporting vessel integrity after neonatal stroke. It was recently reported that there is a higher percentage of microglia associated with the vasculature in healthy postnatal brains compared to adult brains and restriction of microglial migration along vessels when development of astrocyte endfeet surrounding vessels is complete,[32] which may also play a role in the BBB function in neonates. Findings in this study demonstrate that improved functional outcomes in KO are associated with increased vessel interaction with cells of the monocyte lineage are consistent with the latter notion.

Since traditional markers Iba1 and CD68 do not reveal cell identity within the monocyte lineage, microglial cells vs. infiltrated monocytes, and infiltrated monocytes can comprise toxic and beneficial phenotypes, and be of distinct origins,[33] we used multiple markers and flow cytometry to distinguish microglia from monocytes and characterize phenotypes of monocyte-derived macrophages. While the patterns of activation of $TMEM119^{+}$ microglia were similar in injured regions of HET and KO pups, accumulation of toxic $CD11b^{high}/CD45^{high}/Ly6C^{+}/Ly6G^{-}$ monocytes was attenuated in KO. We report that S1PR2 signaling contributes to monocyte infiltration after neonatal stroke. Attenuation of inflammatory cascades induced by toxic monocytes can be important for neuronal preservation and reorganization of neuronal circuits during postnatal brain development. Based on data on enhancing microglial activation and exacerbation of adult stroke by blood-derived monocytes that have infiltrated into ischemic area,[34] it is also plausible to speculate that reduced infiltration of toxic monocytes contributed to protection in our study. The intriguing observation in our study is that despite reduced infiltration of toxic monocytes, the magnitude of tMCAO-induced cytokine and chemokine accumulation in injured regions was essentially unaffected in KO, with exception of significantly reduced MIP-1β and MIP-1α levels. MIP-1 α/β are major drivers of monocytes to injured brain, thus likely contributing to reduced inflammatory monocyte infiltration in KO, but it remains unknown whether the overall unaffected levels of other cytokines and chemokines in injured regions are due to unsynchronized cell-type specific cytokine/chemokine release or particular time of examination.

We used pharmacological S1PR2 inhibition as a more translational strategy in conjunction with the experiments we performed in S1PR2 KO mice. The overall number of reports on effects of selective S1PR2 inhibitor JTE-013 in brain injury is sparse. JTE-013 was shown to attenuate endothelial activation and protect adult mouse from stroke in part by blocking binding of endothelial- or serum-derived S1P to S1PR2 and inhibiting endothelial cell activation,[11] by reducing NfkB activation and attenuating cytokine accumulation during acute stroke.[35] Although JTE-013 is selective for S1PR2, in higher doses it can affect a broad array of mechanisms of sphingolipid metabolism[36] and other signaling pathways implicated in the pathophysiology of stroke, as was shown by its effects in adult S1PR2 KO mice.[37] We show that JTE-013 administration beginning 1 h after reperfusion reduces injury and attenuates caspase-3 mediated neuronal death, the notion supporting beneficial

effects of genetic S1PR2 disruption on outcomes of neonatal stroke. Examination of several mechanisms showed that S1PR2 deletion does not have direct effects on vascular coverage, microglial proliferation, myelination, or neurogenesis after tMCAO in neonates, but our data do not allow us to delineate which members of the S1P signaling pathways and which cell types contribute to the observed protection. In adults, sphingosine kinases (Sphk)½, enzymes that produce S1P and decrease levels of ceramide and sphingosine, are critical for the maintenance of physiological sphingolipid balance and likely have opposite roles in stroke. Sphk1 was shown to contribute to brain inflammation,[38] regulate transport in endothelial cells[39] and NfkB activation in macrophages,[40] while lack/insufficiency of SphK1/S1P signaling can also produce iron overload at the extracellular milieu and lead to lipid peroxidation and neuronal cell death following stroke.[41] Magnitude and particulars of effects of S1PR2 KO were shown to depend on mouse strain with KO on 129/SvEvTacfBR × C57BL/6 with the seventh backcross onto C57BL/6N exhibiting severe early-onset neurological manifestations, including high frequency of spontaneous seizures that occur between P25 and P45 and high mortality levels.[42] Seizures were not apparent in P9-P24 HET and KO mice in this study. Processes mediated by S1PR2 in individual cell types in the injured brain may not be coordinated in time and it is unknown how cell-type specific S1PR2 signaling affects brain injury and repair after neonatal stroke.

Another insufficiently understood aspect is whether observed effects on injury are solely mediated via S1PR2 or whether it is the relative expression of S1PR1 and S1PR2 that determines the outcome. Administration of an S1PR1 agonist FTY720 (fingolimod) effectively attenuated injury in an EAE model, an animal model of multiple sclerosis,[43] predominantly by acting on T cells.[13,44,45] FTY720 was also shown to reduce inflammatory cytokine production and increase neurotrophic factor expression in plated microglia.[46] In stroke, FTY720 decreased the number of microglia/macrophages,[47] induced microglial protective phenotypes,[48] attenuated hemorrhagic transformation,[49] and attenuated memory impairment.[50] In contrast, in neonatal H-I, FTY720 exacerbated brain injury,[51] but prevented injury when LPS was administered before H-I,[12] indicating that beneficial effects of FTY720 on brain injury in neonates require inflammatory priming, including pre-activation of microglia. Endothelial-specific loss of S1PR1 was shown to increase vascular permeability in the lungs[52] whereas S1PR1 agonism attenuated lung ischemia-reperfusion injury.[53] In the current study, we observed a marked reduction in S1PR1 expression in injured regions, but the magnitude of reduction was similar in WT, HET, and KO, making it unlikely that S1PR1 loss or changed S1PR1/S1PR2 balance accounts for the observed effects.

Examination of axonal extension of callosal projection neurons under physiological conditions occurs around P8 and continues to refine until around P21 in mice.[19,20] In our study, the development of cortico-cortical projections, especially in the secondary motor cortex near the infarction area, is affected by both tMCAO and S1PR2 deficiency, as evident from decreased neurofilament myelination in the contralateral cortex, and decreased percent of $FoxP2^{+}$ projection neurons in the ipsilateral cortex.

In summary, this study adds to the knowledge of the inflammatory response as a hallmark of neonatal ischemic brain injury and demonstrates that the features of the immune response mediated by peripheral cells and by microglial cells differ from those in adult stroke. In particular, the findings that elimination of S1PR2 signaling and, as such, modification of lipid and metabolic signaling, improves functional outcome after neonatal stroke is the first step in filling the gap in understanding the interplay within the microglia-leukocyte axis in relation to S1PR-dependent neuroprotection and brain repair.

Limitations of the study

In this study on the role of S1PR2 in brain injury after stroke in neonates, we focused on effects within 2 weeks. It would be important to extend window to young adulthood to identify the long-term effects of S1PR2 deletion. Considering that neurogenesis is not directly affected by S1PR2 deficiency, it would be important to enhance knowledge of cell-type specific S1PR2-mediated effects to appropriately guide the development of therapy for neonatal stroke.

STAR★METHODS

Detailed methods are provided in the online version of this paper and include the following:

- KEY RESOURCES TABLE
- RESOURCE AVAILABILITY
  - Lead contact
  - Materials availability

SUPPLEMENTAL INFORMATION

Supplemental information can be found online at https://doi.org/10.1016/j.isci.2023.106340.

ACKNOWLEDGMENTS

The work was supported by R01 HL139685 (Z.V.), RO1 NS44025 (Z.V.), and RO1 NS76726 (Z.V.).

AUTHOR CONTRIBUTIONS

Y.F. performed experiments, analyzed data, and wrote the manuscript; J.F. and M.L. performed experiments, analyzed data, and contributed to writing the manuscript; A.R. performed experiments and contributed to writing the manuscript; Z.V. funded the study, designed and oversaw the study, analyzed data, and wrote the manuscript.

DECLARATION OF INTERESTS

The authors declare no conflicts.

Received: August 2, 2022
Revised: October 31, 2022
Accepted: March 1, 2023
Published: March 5, 2023

REFERENCES

1. Murphy, T.H., and Corbett, D. (2009). Plasticity during stroke recovery: from synapse to behaviour. Nat. Rev. Neurosci. *10*, 861–872. https://doi.org/10.1038/nrn2735.

2. Su, F., and Xu, W. (2020). Enhancing brain plasticity to promote stroke recovery. Front. Neurol. *11*, 554089. https://doi.org/10.3389/fneur.2020.554089.

3. Tagawa, Y., Kanold, P.O., Majdan, M., and Shatz, C.J. (2005). Multiple periods of functional ocular dominance plasticity in mouse visual cortex (2005). Nat. Neurosci. *8*, 380–388. https://doi.org/10.1038/nn1410.

4. Hagberg, H., Mallard, C., Ferriero, D.M., Vannucci, S.J., Levison, S.W., Vexler, Z.S., and Gressens, P. (2015). The role of inflammation in perinatal brain injury (2015). Nat. Rev. Neurol. *11*, 192–208. https://doi.org/10.1038/nrneurol.2015.13.

5. Kirton, A., Metzler, M.J., Craig, B.T., Hilderley, A., Dunbar, M., Giuffre, A., Wrightson, J., Zewdie, E., and Carlson, H.L. (2021). Perinatal stroke: mapping and modulating developmental plasticity (2021). Nat. Rev. Neurol. *17*, 415–432. https://doi.org/10.1038/s41582-021-00503-x.

6. Fernández-López, D., Faustino, J., Daneman, R., Zhou, L., Lee, S.Y., Derugin, N., Wendland, M.F., and Vexler, Z.S. (2012). Blood-brain barrier permeability is increased after acute adult stroke but not neonatal stroke in the rat. J. Neurosci. *32*, 9588–9600. https://doi.org/10.1523/JNEUROSCI.5977-11.2012.

7. Woo, M.S., Wang, X., Faustino, J.V., Derugin, N., Wendland, M.F., Zhou, P., Iadecola, C., and Vexler, Z.S. (2012). Genetic deletion of CD36 enhances injury after acute neonatal stroke. Ann. Neurol. *72*, 961–970.

8. Fernández-López, D., Faustino, J., Klibanov, A.L., Derugin, N., Blanchard, E., Simon, F., Leib, S.L., and Vexler, Z.S. (2016). Microglial cells prevent hemorrhage in neonatal focal arterial stroke. J. Neurosci. *36*, 2881–2893. https://doi.org/10.1523/JNEUROSCI.0140-15.2016.

9. Rayasam, A., Faustino, J., Lecuyer, M., and Vexler, Z.S. (2020). Neonatal stroke and TLR1/2 ligand recruit myeloid cells through the choroid plexus in a CX3CR1-CCR2- and context-specific manner. J. Neurosci. *40*, 3849–3861. https://doi.org/10.1523/JNEUROSCI.2149-19.2020.

10. Rayasam, A., Fukuzaki, Y., and Vexler, Z.S. (2021). Microglia-leucocyte axis in cerebral ischaemia and inflammation in the developing brain. Acta Physiol. *233*, e13674. https://doi.org/10.1111/apha.13674.

11. Kim, G.S., Yang, L., Zhang, G., Zhao, H., Selim, M., McCullough, L.D., Kluk, M.J., and Sanchez, T. (2015). Critical role of sphingosine-1-phosphate receptor-2 in the disruption of cerebrovascular integrity in experimental stroke. Nat. Commun. *6*, 7893. https://doi.org/10.1038/ncomms8893.

12. Yang, D., Sun, Y.Y., Bhaumik, S.K., Li, Y., Baumann, J.M., Lin, X., Zhang, Y., Lin, S.H., Dunn, R.S., Liu, C.Y., et al. (2014). Blocking lymphocyte trafficking with FTY720 prevents inflammation-sensitized hypoxic-ischemic brain injury in newborns. J. Neurosci. *34*, 16467–16481. https://doi.org/10.1523/JNEUROSCI.2582-14.2014.

13. Cartier, A., and Hla, T. (2019). Sphingosine 1-phosphate: Lipid signaling in pathology and therapy. Science *366*. https://doi.org/10.1126/science.aar5551.

14. Thuy, A.V., Reimann, C.M., Hemdan, N.Y.A., and Gräler, M.H. (2014). Sphingosine

1-phosphate in blood: function, metabolism, and fate. Cell. Physiol. Biochem. *34*, 158–171. https://doi.org/10.1159/000362992.

15. Faustino, J.V., Wang, X., Johnson, C.E., Klibanov, A., Derugin, N., Wendland, M.F., and Vexler, Z.S. (2011). Microglial cells contribute to endogenous brain defenses after acute neonatal focal stroke. J. Neurosci. *31*, 12992–13001. https://doi.org/10.1523/JNEUROSCI.2102-11.2011.

16. Chip, S., Fernández-López, D., Li, F., Faustino, J., Derugin, N., and Vexler, Z.S. (2017). Genetic deletion of galectin-3 enhances neuroinflammation, affects microglial activation and contributes to sub-chronic injury in experimental neonatal focal stroke. Brain Behav. Immun. *60*, 270–281. https://doi.org/10.1016/j.bbi.2016.11.005.

17. Chumak, T., Lecuyer, M.J., Nilsson, A.K., Faustino, J., Ardalan, M., Svedin, P., Sjöbom, U., Ek, J., Obenaus, A., Vexler, Z.S., and Mallard, C. (2022). Maternal n-3 polyunsaturated fatty acid enriched diet commands fatty acid composition in postnatal brain and protects from neonatal arterial focal stroke. Transl. Stroke Res. *13*, 449–461. https://doi.org/10.1007/s12975-021-00947-9.

18. Aghaeepour, N., Finak, G., FlowCAP Consortium; DREAM Consortium, Hoos, H., Mosmann, T.R., Brinkman, R., Gottardo, R., and Scheuermann, R.H. (2013). Critical assessment of automated flow cytometry data analysis techniques. Nat. Methods *10*, 228–238. https://doi.org/10.1038/nmeth.2365.

19. Shepherd, G.M.G., and Yamawaki, N. (2021). Untangling the cortico-thalamo-cortical loop: cellular pieces of a knotty circuit puzzle. Nat. Rev. Neurosci. *22*, 389–406. https://doi.org/10.1038/s41583-021-00459-3.

20. Fame, R.M., MacDonald, J.L., and Macklis, J.D. (2011). Development, specification, and diversity of callosal projection neurons. Trends Neurosci. *34*, 41–50. https://doi.org/10.1016/j.tins.2010.10.002.

21. Wacker, B.K., Freie, A.B., Perfater, J.L., and Gidday, J.M. (2012). Junctional protein regulation by sphingosine kinase 2 contributes to blood-brain barrier protection in hypoxic preconditioning-induced cerebral ischemic tolerance. J. Cerebr. Blood Flow Metabol. *32*, 1014–1023. https://doi.org/10.1038/jcbfm.2012.3jcbfm20123.

22. Zhang, G., Yang, L., Kim, G.S., Ryan, K., Lu, S., O'Donnell, R.K., Spokes, K., Shapiro, N., Aird, W.C., Kluk, M.J., et al. (2013). Critical role of sphingosine-1-phosphate receptor 2 (S1PR2) in acute vascular inflammation. Blood *122*, 443–455. https://doi.org/10.1182/blood-2012-11-467191.

23. Wood, T., Osredkar, D., Puchades, M., Maes, E., Falck, M., Flatebø, T., Walløe, L., Sabir, H., and Thoresen, M. (2016). Treatment temperature and insult severity influence the neuroprotective effects of therapeutic hypothermia. Sci. Rep. *6*, 23430. https://doi.org/10.1038/srep23430.

24. Johnston, M.V., and Hagberg, H. (2007). Sex and the pathogenesis of cerebral palsy. Dev. Med. Child Neurol. *49*, 74–78.

25. Nuñez, J. (2012). Sex and steroid hormones in early brain injury. Rev. Endocr. Metab. Disord. *13*, 173–186. https://doi.org/10.1007/s11154-012-9219-3.

26. Hagberg, H., Wilson, M.A., Matsushita, H., Zhu, C., Lange, M., Gustavsson, M., Poitras, M.F., Dawson, T.M., Dawson, V.L., Northington, F., and Johnston, M.V. (2004). PARP-1 gene disruption in mice preferentially protects males from perinatal brain injury. J. Neurochem. *90*, 1068–1075.

27. Renolleau, S., Fau, S., and Charriaut-Marlangue, C. (2008). Gender-related differences in apoptotic pathways after neonatal cerebral ischemia. Neuroscientist *14*, 46–52.

28. Nijboer, C.H.A., Groenendaal, F., Kavelaars, A., Hagberg, H.H., van Bel, F., and Heijnen, C.J. (2007). Gender-specific neuroprotection by 2-iminobiotin after hypoxia-ischemia in the neonatal rat via a nitric oxide independent pathway. J. Cerebr. Blood Flow Metabol. *27*, 282–292.

29. Fleiss, B., Nilsson, M.K.L., Blomgren, K., and Mallard, C. (2012). Neuroprotection by the histone deacetylase inhibitor trichostatin A in a model of lipopolysaccharide-sensitised neonatal hypoxic-ischaemic brain injury. J. Neuroinflammation *9*, 70. https://doi.org/10.1186/1742-2094-9-70 1742-2094-9-70.

30. Braun, A., Xu, H., Hu, F., Kocherlakota, P., Siegel, D., Chander, P., Ungvari, Z., Csiszar, A., Nedergaard, M., and Ballabh, P. (2007). Paucity of pericytes in germinal matrix vasculature of premature infants. J. Neurosci. *27*, 12012–12024. https://doi.org/10.1523/JNEUROSCI.3281-07.2007.27/44/12012.

31. Koizumi, T., Kerkhofs, D., Mizuno, T., Steinbusch, H.W.M., and Foulquier, S. (2019). Vessel-associated immune cells in cerebrovascular diseases: from perivascular macrophages to vessel-associated microglia. Front. Neurosci. *13*, 1291. https://doi.org/10.3389/fnins.2019.01291.

32. Mondo, E., Becker, S.C., Kautzman, A.G., Schifferer, M., Baer, C.E., Chen, J., Huang, E.J., Simons, M., and Schafer, D.P. (2020). A developmental analysis of juxtavascular microglia dynamics and interactions with the vasculature. J. Neurosci. *40*, 6503–6521. https://doi.org/10.1523/jneurosci.3006-19.2020.

33. Cugurra, A., Mamuladze, T., Rustenhoven, J., Dykstra, T., Beroshvili, G., Greenberg, Z.J., Baker, W., Papadopoulos, Z., Drieu, A., Blackburn, S., and Kanamori, M. (2021). Skull and vertebral bone marrow are myeloid cell reservoirs for the meninges and CNS parenchyma. Science *373*, abf7844. https://doi.org/10.1126/science.abf7844.

34. Werner, Y., Mass, E., Ashok Kumar, P., Ulas, T., Händler, K., Horne, A., Klee, K., Lupp, A., Schütz, D., Saaber, F., et al. (2020). Cxcr4 distinguishes HSC-derived monocytes from microglia and reveals monocyte immune responses to experimental stroke. Nat. Neurosci. *23*, 351–362. https://doi.org/10.1038/s41593-020-0585-y.

35. Sapkota, A., Gaire, B.P., Kang, M.G., and Choi, J.W. (2019). S1P2 contributes to microglial activation and M1 polarization following cerebral ischemia through ERK1/2 and JNK. Sci. Rep. *9*, 12106. https://doi.org/10.1038/s41598-019-48609-z.

36. Pitman, M.R., Lewis, A.C., Davies, L.T., Moretti, P.A.B., Anderson, D., Creek, D.J., Powell, J.A., and Pitson, S.M. (2022). The sphingosine 1-phosphate receptor 2/4 antagonist JTE-013 elicits off-target effects on sphingolipid metabolism. Sci. Rep. *12*, 454. https://doi.org/10.1038/s41598-021-04009-w.

37. Salomone, S., and Waeber, C. (2011). Selectivity and specificity of sphingosine-1-phosphate receptor ligands: caveats and critical thinking in characterizing receptor-mediated effects. Front. Pharmacol. *2*, 9. https://doi.org/10.3389/fphar.2011.00009.

38. Grin'kina, N.M., Karnabi, E.E., Damania, D., Wadgaonkar, S., Muslimov, I.A., and Wadgaonkar, R. (2012). Sphingosine kinase 1 deficiency exacerbates LPS-induced neuroinflammation. PLoS One *7*, e36475. https://doi.org/10.1371/journal.pone.0036475.

39. Pilorget, A., Demeule, M., Barakat, S., Marvaldi, J., Luis, J., and Béliveau, R. (2007). Modulation of P-glycoprotein function by sphingosine kinase-1 in brain endothelial cells. J. Neurochem. *100*, 1203–1210. https://doi.org/10.1111/j.1471-4159.2006.04295.x.

40. Wu, W., Mosteller, R.D., and Broek, D. (2004). Sphingosine kinase protects lipopolysaccharide-activated macrophages from apoptosis. Mol. Cell Biol. *24*, 7359–7369. https://doi.org/10.1128/MCB.24.17.7359-7369.2004.

41. DeGregorio-Rocasolano, N., Martí-Sistac, O., and Gasull, T. (2019). Deciphering the iron side of stroke: neurodegeneration at the crossroads between iron dyshomeostasis, excitotoxicity, and ferroptosis. Front. Neurosci. *13*, 85. https://doi.org/10.3389/fnins.2019.00085.

42. Akahoshi, N., Ishizaki, Y., Yasuda, H., Murashima, Y.L., Shinba, T., Goto, K., Himi, T., Chun, J., and Ishii, I. (2011). Frequent spontaneous seizures followed by spatial working memory/anxiety deficits in mice lacking sphingosine 1-phosphate receptor 2. Epilepsy Behav. *22*, 659–665. https://doi.org/10.1016/j.yebeh.2011.09.002.

43. Smith, P.A., Schmid, C., Zurbruegg, S., Jivkov, M., Doelemeyer, A., Theil, D., Dubost, V., and Beckmann, N. (2018). Fingolimod inhibits brain atrophy and promotes brain-derived neurotrophic factor in an animal model of multiple sclerosis. J. Neuroimmunol. *318*, 103–113. https://doi.org/10.1016/j.jneuroim.2018.02.016.

44. Garris, C.S., Blaho, V.A., Hla, T., and Han, M.H. (2014). Sphingosine-1-phosphate receptor 1 signalling in T cells: trafficking and beyond. Immunology *142*, 347–353. https://doi.org/10.1111/imm.12272.

45. Rivera, J., Proia, R.L., and Olivera, A. (2008). The alliance of sphingosine-1-phosphate and its receptors in immunity. Nat. Rev. Immunol. *8*, 753–763. https://doi.org/10.1038/nri2400.

46. Noda, H., Takeuchi, H., Mizuno, T., and Suzumura, A. (2013). Fingolimod phosphate promotes the neuroprotective effects of microglia. J. Neuroimmunol. *256*, 13–18. https://doi.org/10.1016/j.jneuroim.2012.12.005.

47. Czech, B., Pfeilschifter, W., Mazaheri-Omrani, N., Strobel, M.A., Kahles, T., Neumann-Haefelin, T., Rami, A., Huwiler, A., and Pfeilschifter, J. (2009). The immunomodulatory sphingosine 1-phosphate analog FTY720 reduces lesion size and improves neurological outcome in a mouse model of cerebral ischemia. Biochem. Biophys. Res. Commun. *389*, 251–256. https://doi.org/10.1016/j.bbrc.2009.08.142.

48. Shang, K., He, J., Zou, J., Qin, C., Lin, L., Zhou, L.Q., Yang, L.L., Wu, L.J., Wang, W., Zhan, K.B., and Tian, D.S. (2020). Fingolimod promotes angiogenesis and attenuates ischemic brain damage via modulating microglial polarization. Brain Res. *1726*, 146509. https://doi.org/10.1016/j.brainres.2019.146509.

49. Salas-Perdomo, A., Miró-Mur, F., Gallizioli, M., Brait, V.H., Justicia, C., Meissner, A., Urra, X., Chamorro, A., and Planas, A.M. (2019). Role of the S1P pathway and inhibition by fingolimod in preventing hemorrhagic transformation after stroke. Sci. Rep. *9*, 8309. https://doi.org/10.1038/s41598-019-44845-5.

50. Nazari, M., Keshavarz, S., Rafati, A., Namavar, M.R., and Haghani, M. (2016). Fingolimod (FTY720) improves hippocampal synaptic plasticity and memory deficit in rats following focal cerebral ischemia. Brain Res. Bull. *124*, 95–102. https://doi.org/10.1016/j.brainresbull.2016.04.004.

51. Herz, J., Köster, C., Crasmöller, M., Abberger, H., Hansen, W., Felderhoff-Müser, U., and Bendix, I. (2018). Peripheral T cell depletion by FTY720 exacerbates hypoxic-ischemic brain injury in neonatal mice. Front. Immunol. *9*, 1696. https://doi.org/10.3389/fimmu.2018.01696.

52. Knipe, R.S., Spinney, J.J., Abe, E.A., Probst, C.K., Franklin, A., Logue, A., Giacona, F., Drummond, M., Griffith, J., Brazee, P.L., et al. (2022). Endothelial-specific loss of sphingosine-1-phosphate receptor 1 increases vascular permeability and exacerbates bleomycin-induced pulmonary fibrosis. Am. J. Respir. Cell Mol. Biol. *66*, 38–52. https://doi.org/10.1165/rcmb.2020-0408OC.

53. Stone, M.L., Sharma, A.K., Zhao, Y., Charles, E.J., Huerter, M.E., Johnston, W.F., Kron, I.L., Lynch, K.R., and Laubach, V.E. (2015). Sphingosine-1-phosphate receptor 1 agonism attenuates lung ischemia-reperfusion injury. Am. J. Physiol. Lung Cell Mol. Physiol. *308*, L1245–L1252. https://doi.org/10.1152/ajplung.00302.2014.

STAR★METHODS

KEY RESOURCES TABLE

REAGENT or RESOURCE	SOURCE	IDENTIFIER
Antibodies		
Pacific Blue™ anti-mouse CD45	Biolegend	103126
APC anti-mouse Ly-6C	Biolegend	128016
Alexa Fluor® 700 anti-mouse Ly-6G	Biolegend	127622
APC/Cyanine7 anti-mouse/human CD11b	Biolegend	101226
Tmem119 Monoclonal Antibody (V3RT1GOsz), PE	eBioscience	12-6119-80
Alexa Fluor® 488 anti-mouse CD68 Antibody	Biolegend	137012
PE anti-mouse/human CD44 Antibody	Biolegend	103023
FITC anti-mouse CD192 (CCR2) Antibody	Biolegend	150608
PE anti-mouse CD192 (CCR2) Antibody	Biolegend	150609
Alexa Fluor® 488 anti-mouse CX3CR1 Antibody	Biolegend	149022
PE anti-mouse CD8a Antibody	Biolegend	100708
CD11c Monoclonal Antibody (N418), FITC	eBioscience	11-0114-82
GFAP Antibody (PA1-10004) in IHC	Invitrogen	PA1 10004
Anti-NeuN Antibody, clone A60	Sigma	MAB377
Anti-FOXP2 antibody	abcam	Ab16046
Anti Iba1, Rabbit (for Immunocytochemistry)	Wako	019-19741
CD68 antibody | FA-11	BIO-RAD	MCA1957GA
Anti-BrdU antibody [BU1/75 (ICR1)]	Abcam	Ab6326
Cleaved Caspase-3 (Asp175) (5A1E) Rabbit mAb	Cell Signaling	9664S
Anti-Neurofilament 200 antibody produced in rabbit	Sigma	N4142
Anti-Myelin Basic Protein antibody	Abcam	ab134018
Anti-Spectrin alpha chain (nonerythroid) Antibody	Sigma	MAB1622
Monoclonal Anti-β-Actin antibody produced in mouse	Sigma	A5441
S1PR1/EDG1 Polyclonal Antibody	Proteintech	55133
m-IgGκ BP-HRP	Santa Cruz	sc-516102
anti-rabbit IgG-HRP	Santa Cruz	sc-2357
Goat anti-Rabbit IgG (H+L) Highly Cross-Adsorbed Secondary Antibody, Alexa Fluor™ 488	Thermo	A11034
Goat anti-Rat IgG (H+L) Cross-Adsorbed Secondary Antibody, Alexa Fluor™ 488	Thermo	A11006
Goat anti-Mouse IgG (H+L) Highly Cross-Adsorbed Secondary Antibody, Alexa Fluor™ 488	Thermo	A11029
Goat anti-Chicken IgY (H+L) Secondary Antibody, Alexa Fluor™ 488	Thermo	A11039
Goat anti-Rabbit IgG (H+L) Cross-Adsorbed Secondary Antibody, Alexa Fluor™ 568	Thermo	A11011
Goat anti-Mouse IgG (H+L) Highly Cross-Adsorbed Secondary Antibody, Alexa Fluor™ 568	Thermo	A11031
Goat anti-Chicken IgY (H+L) Secondary Antibody, Alexa Fluor™ 568	Thermo	A11041

(*Continued on next page*)

Continued

REAGENT or RESOURCE	SOURCE	IDENTIFIER
Goat anti-Rabbit IgG (H+L) Highly Cross-Adsorbed Secondary Antibody, Alexa Fluor™ 647	Thermo	A21245
Goat Anti-Rat IgG H&L (Alexa Fluor® 647)	Abcam	ab150167
Chemicals, peptides, and recombinant proteins		
JTE-013	Cayman	10009458
Antigen Unmasking Solution, Citrate-Based	Vector	H-3300
M.O.M.® (Mouse on Mouse) Blocking Reagent	Vector	MKB-2213
CollagenaseD	Roche	11088866001
TrueBlack Lipofuscin Autofluorescence Quencher	Biotium	23007
PefablocSC	Roche	11429868001
NuPAGE™ Sample Reducing Agent	Invitrogen	NP0009
cOmplete™ ULTRA Tablets, Protease Inhibitor Cocktail	Roche	5892970001
4–12% SDS-polyacrylamide gels	Invitrogen	NW04125
Western Blot Stripping Buffer	Thermo	46430
2-Hpβc	Cayman	16169
Bio-Plex Pro Mouse Cytokine 23-plex Assay	Bio-Rad	M60009RDPD
Cell Lysis Buffer (10X)	Cell Signaling	9803
Percoll	Sigma	P1644
Fetal Bovine Serum, qualified	Gibco	16140071
EDTA (0.5 M), pH 8.0, RNase-free	Invitrogen	AM9260G
RPMI Medium	Gibco	11875085
Pierce™ BCA Protein Assay Kit	Thermo Scientific	23227
TruStain FcX™ (anti-mouse CD16/32) FcBlock	Biolegend	101320
ProLong™ Gold Antifade Mountant	Thermo	P36930
Pierce ECL western blotting substrate	Thermo	32106
Experimental models: Organisms/strains		
S1PR2 KO (129/SvEvTacfBR × C57BL/6)	N/A	MGI: 3620009
Software and algorithms		
Carl Zeiss Axiovert 100 equipped with Volocity Software	Improvision/PerkinElmer	N/A
LSR Fortessa.	BD	N/A
FlowJo software	Tree Star	N/A
Kinovia	Kinovia	N/A
StatLIA software	Brendan Scientific	N/A
ImageJ	NIH	N/A
Prism 9	GraphPad	N/A
BioRender illustrations	BioRender	N/A

RESOURCE AVAILABILITY

Lead contact

Further information and requests for resources and reagents should be directed to and will be fulfilled by the lead contact, Zinaida Vexler (Zena.Vexler@ucsf.edu).

Materials availability

This study did not generate new unique reagents.

Data and code availability

- Data reported in this paper will be shared by the lead contact upon request.
- This paper does not report original code.
- Any additional information required to reanalyze the data reported in this paper is available from the lead contact upon request.

EXPERIMENTAL MODEL AND SUBJECT DETAILS

Animals

All research conducted on animals was approved by the University of California San Francisco Institutional Animal Care and Use Committee and in accordance with the Guide for the care and use of laboratory animals (U.S. Department of Health and Human Services). Animals were given *ad libitum* access to food and water, housed with nesting material and shelters, and kept in rooms with temperature control and light/dark cycles. The data are in compliance with STAR and ARRIVE guidelines (Animal Research: Reporting *in Vivo* Experiments). Block litter design and randomization within individual litters were used. Blinded data analysis was used where possible.

Model of ischemia-reperfusion in neonatal mice

A 3h tMCAO was performed on postnatal day 9 (P9)-P10 male and female WT (n = 32), HET (n = 105) and KO (n = 71) pups, all on C57Bl/6 background, as we previously described.[7] Briefly, a midline cervical incision was made under isoflurane anesthesia, the common carotid artery and internal carotid artery exposed, single threads from a 7-0 silk suture used to temporary tie a knot below the origin of the internal carotid artery to prevent retrograde bleeding from the arteriotomy. A coated 7-0 nylon suture was advanced 4–5 mm and removed 3h later. Mortality rates were 5.71% (HET) and 4.23% (KO). Mice from the same litter were randomized to receive tMCAO or sham surgery. In sham-operated pups, suture was inserted but not advanced. During surgical procedure and post-surgery temperature was maintained with temperature-controlled pad.

Histology and immunofluorescence

Animals were perfused and brains postfixed with 4% PFA, post-fixed, cryoprotected, and flash-frozen brains were sectioned on a cryostat (12-μm-thick serial sections, 360μm apart) and volume of hemispheres ipsilateral and contralateral to tMCAO to assess brain edema and volumes of injured regions determined in 8 coronal Nissl-stained sections were measured in blinded manner. Immunofluorescence was performed on adjacent sections permeabilized with 0.3% Triton-X100 for 1h followed by quenching with TrueBlack Lipofuscin Autofluorescence Quencher (Biotium, #23007) to reduce autofluorescence in injured regions and blocked in 20% normal goat sera and M.O.M blocking reagent (Vector, MKB-2213-1) in PBS. Slides were incubated overnight in 5% NGS in PBS with primary antibodies; rabbit anti-Iba1(1:200, Wako), mouse anti-Glut1 (1:300, Abcam), rabbit anti-cleaved caspase 3 (1:100 Cell signaling), rat anti-CD68 (1:200, Biorad), mouse anti-NeuN (1:200), rabbit anti-NF(1:400), chicken anti MBP (1:500), rat anti-BrdU (1:200, Abcam) and chicken anti GFAP (1:1000, Invitrogen), followed by appropriate secondary antibodies (Invitrogen), incubation with DAPI, and mounting using coverslips with ProLong Gold (Invitrogen).

BrdU (5 μl/g weight of 10 mg/mL solution) was injected 3 times (twice per day, i.p.), starting at P22. For BrdU staining, slides were incubated in sodium citrate (95°C, 1 min), 2N HCl (37°C, 30 min), and 0.1M boric acid (10 min, RT) before blocking. Z stacks of 8 images were captured at 1.0 μm intervals (25×/100× oil objectives, Carl Zeiss Axiovert 100 equipped with Volocity Software, Improvision/PerkinElmer) and analysis performed in perifocal injury region and in two fields-of-view (FOV) in the ischemic core (FOV3 and FOV4) and in matching contralateral regions using automated protocols for signal intensity threshold, which was set >2SD background in each channel.

Flow cytometry

Mice deeply anesthetized with isoflurane were transcardially perfused with cold PBS, brain tissue removed, minced with razor blades, washed with RPMI, and incubated in 1 mg/mL collagenase D for 45 min at 37°C with shaking. 5 mM EDTA was added to inhibit enzymatic reaction during last 5 min. Cells were washed with RPMI, resuspended in 70% Percoll, and overlaid with 30% Percoll, and centrifuged at 2500 rpm for 30 min at

4°C without brake. Pellet between layers was collected and washed twice with FACS buffer (2% FBS, 1 mM EDTA, in PBS, Mg2+ Ca2+ Free). Resuspended cells were incubated with Fc Blocking (Biolegend#101320) for 20min followed by staining for 1h on ice with the following antibodies: CD45-Pacific Blue (Biolegend), CD11b-APC-Cy7 (Biolegend), Ly6g (IA8)-AF700 (Biolegend), Ly6c (Hk1.4)- APC (Biolegend), Tmem119-PE (eBioscience), CD68-FITC, CD44-PE (Biolegend), CCR2-FITC (Biolegend), CCR2-PE (Biolegend), CX3CR1-FITC (Biolegend), CD8a-PE (Biolegend) and CD11c-FITC (Biolegend), 1:200 or 1:100. Fluorescence Minus One (FMO) samples were applied, which is a commonly used strategy to prevent false-positive results through overlap of fluorophores.[18] Cells were washed 2 times in FACS buffer and evaluated using BD LSR Fortessa. Data analysis was performed using FlowJo software (Tree Star).

Western blot analysis

Whole cortical lysates from contralateral and injured cortical regions were obtained from mice perfused intracardially with 5 ml of cold PBS followed by rapid tissue dissection and snap-freezing. Tissue was homogenized in lysis buffer (Cell Signaling Technology, #9803) and NuPAGE™ Sample Reducing Agent (Invitrogen, #NP0009) supplemented with protease inhibitor cocktail (Roche, #5892970001) and 1 mM PefablocSC (Roche, #11429868001). Proteins were separated on 4–12% SDS-polyacrylamide gels (Invitrogen, # NW04125). The membranes were blocked for 1 h in 5% nonfat dry milk in TBST (20 mM Tris-HCl, 150 mM NaCl, 0.1% Tween 20), incubated overnight at 4 °C with the following primary antibodies: spectrin (1:1000, Sigma #MAB1622), beta-actin (1:4000, Sigma #A5441), S1PR1 (1:500, Proteintech, #55133) and, subsequently, with secondary antibodies, mouse anti-rabbit IgG-HRP (#sc-2357), m-IgGκ BP-HRP (#sc-516102) for 1 h at RT, following washes in TBST. The bound antibodies were removed from membranes with stripping buffer (Thermo, #46430).

Multiplex cytokine assay

Whole cortical lysates from contralateral and injured cortical regions were obtained from mice perfused intracardially with 5 ml of cold PBS followed by rapid tissue dissection and snap-freezing. Tissue was homogenized in Lysis buffer (20 mM Tris, 150 mM NaCl, 0.05% Tween20 in PBS) supplemented with protease inhibitor cocktail (Roche, #5892970001) and PefablocSC (Roche, #11429868001). Measurements were performed using Bio-Plex Pro Mouse Cytokine 23-plex Assay (Bio-Rad, #M60009RDPD) and StatLIA software (Brendan Scientific) with a 5-parameter logistic curve fitting. The data were normalized to protein concentration in the same brain homogenate sample.

JTE-013 solution preparation and administration

JTE-013 (Cayman, #10009458) was dissolved in 30 mg/ml of 2-Hpβc (2-Hydroxypropyl-β-cyclodextrin (Cayman, cat #16169) containing 10% ethanol immediately before injections and warm solution administered to avoid precipitation. Two doses were tested, 2.5 μg/g and 5 μg/g (i.p., beginning at 1h of reperfusion followed by single daily injections, volume of respective 1.25 μg/μl and 2.5 μg/μl solution was adjusted per animal weight). Vehicle solution contained 30 mg/ml of 2-Hpβc containing 10% ethanol.

Open field test

Open Field test was used to measure locomotor activity and anxious behavior. The mice were placed in the center of the cage (30 cm x 40 cm, 8 x 8 grid pattern) and trajectory was video recorded from the top for 3 min for P10 and 5 min for P21. Mouse movement was video-tracked using Kinovia, total traveling distance and percentage of distance in the center area (4 x 4 in grid pattern) was measured by ImageJ (NIH) following noise removal. Self-grooming time and number of rearings (stands on its hind legs) were counted during same time duration.

QUANTIFICATION AND STATISTICAL ANALYSIS

Block litter design was used to avoid litter-to-litter variability and randomization of pups for tMCAO/naive was used where possible. Injury analysis was performed in a blinded manner. Mice from the same litter were randomized to receive tMCAO surgery and were either sacrificed for biochemical measurements at 72h or for histological outcomes at two time points, 72h or 2 weeks. Most of WT and KO mice underwent behavior testing 24h after reperfusion. Assignment of mice to "Severe Injury" group and "Mild Injury" groups was done based on the pattern observed at the time of sacrifice, i.e., the presence of gross injury in the cortex. Each dot on all graphs represents an individual mouse. Results are shown as mean ± SD. Outliers were

identified based on 2SD criteria. Normality of data distribution was tested with the Shapiro-Wilk test. One-way ANOVA followed by Brown-Forsythe and Welch ANOVA was used to compare multiple groups, two-way ANOVA was used to compare multiple groups with independent variables followed by two-stage step-up method of Benjamini, Krieger and Yekutieli, and *t*-test (parametric) or Mann Whitney test (nonparametric) analysis was used to compared two groups. Particular tests used are described in legends to individual figures. GraphPad Prism 9 software was used to generate statistical data.